

Relaxation of capillary-gravity waves due to contact line nonlinearity: A projection method

Cite as: Chaos **31**, 123124 (2021); <https://doi.org/10.1063/5.0055898>

Submitted: 04 May 2021 • Accepted: 24 November 2021 • Published Online: 20 December 2021

 Alessandro Bongarzone,  Francesco Viola and  François Gallaire



View Online



Export Citation



CrossMark

Scilight

Summaries of the latest breakthroughs
in the **physical sciences**



Relaxation of capillary-gravity waves due to contact line nonlinearity: A projection method

Cite as: Chaos 31, 123124 (2021); doi: 10.1063/5.0055898

Submitted: 4 May 2021 · Accepted: 24 November 2021 ·

Published Online: 20 December 2021



View Online



Export Citation



CrossMark

Alessandro Bongarzone,¹ Francesco Viola,² and François Gallaire^{1,a)}

AFFILIATIONS

¹Laboratory of Fluid Mechanics and Instabilities, École Polytechnique Fédérale de Lausanne, Lausanne CH-1015, Switzerland

²Gran Sasso Science Institute, Viale F. Crispi, 7, 67100 L'Aquila, Italy

^{a)}Author to whom correspondence should be addressed: francois.gallaire@epfl.ch

ABSTRACT

We present a physics-inspired mathematical model based on successive linear eigenmode projections to solve the relaxation of small-amplitude and two-dimensional viscous capillary-gravity waves with a phenomenological nonlinear contact line model. We show that each projection eventually induces a rapid loss of total energy in the liquid motion and contributes to its nonlinear damping.

Published under an exclusive license by AIP Publishing. <https://doi.org/10.1063/5.0055898>

The comprehension of the role of wetting properties in the damping of liquid oscillations in confined basins is a long-standing problem in the hydrodynamics field and for which renewed interest has emerged in recent years. A series of careful lab-scale experiments have revealed that the damping of liquid natural small oscillations varies nonlinearly with the oscillation amplitude, in contrast with previous theoretical predictions,^{1–4} which prescribe a constant and unique value for the damping rate, thus indicating a dependence on the contact line behavior and hence on the solid substrate material. This effect has been tentatively attributed to a source of dissipation localized in the proximity of the air–liquid–solid triple line, which, during the dynamics, may exhibit a complex hysteretic behavior under the effect of a solid-like wall friction. In this work, assuming that the contact line behaves according to experimentally inspired phenomenological laws, we formalize a mathematical method based on successive linear eigenmode projections for solving numerically the nonlinear fluid motion in the limit of small oscillation amplitudes. This approach captures the transition from a contact line stick-slip (or nearly stick-slip) motion to a pinned (or nearly pinned) configuration, as well as the secondary fluid bulk motion following the arrest of the contact line, overlooked by previous asymptotic analyses.

I. INTRODUCTION

Sloshing motion is an archetypal damped oscillator in fluid mechanics. Originally, the eigenfrequencies of standing

capillary-gravity waves in closed basins were derived in the potential flow limit,¹ while the linear viscous dissipation at the free-surface at the solid walls and in the bulk for low-viscosity fluids was typically accounted for by a boundary layer approximation.^{2–4} This classic theoretical approach is built on the simplifying assumption that the free liquid surface, η , intersects the lateral wall orthogonally, and the contact line can freely slip with constant zero slope, $\partial_n \eta = 0$ (free-end edge condition), where ∂_n is the spatial derivative in the direction normal to the lateral wall.

Although this hypothesis is reasonable in gravity dominated waves within large containers, several laboratory-size experiments^{2,5–8} have unveiled that the values of damping rates predicted by the viscous theory are considerably underestimated, owing to the nonlinear dependence of the damping rate on the oscillation amplitude and, therefore, indicating a non-negligible influence of the lateral wall material and wetting properties.^{2,6} In such cases, where capillary effects at the wall are relevant, the wave frequency and the damping rate are sensitive to the contact line boundary condition and the free-end edge condition does not provide the complex relation between the contact line speed and the macroscopic contact angle observed experimentally, with the latter oscillating around its static value, θ_s , alternating between two values, θ_a and θ_r , corresponding to an advancing and a receding contact line, respectively, and hence exhibiting hysteresis^{4,7–10} [see Fig. 1(a)]. The dynamic variation of the contact angle with the contact line speed, which we here refer to as dynamic hysteresis, has been attributed to the liquid's inability to flow over a solid substrate.^{11–13} On the other hand, the difference between the advancing and receding contact

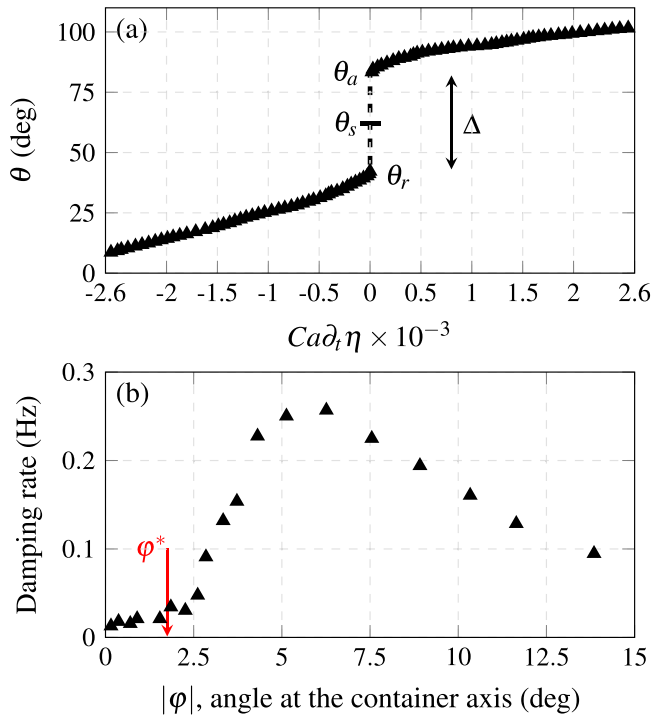


FIG. 1. (a) Experimental contact line model proposed in Fig. 3 of Ref. 8 for water oscillations in a cylindrical container. Here, the capillary number is defined as $Ca = \mu \sqrt{gR}/\gamma$, where ρ is the fluid density, μ is the dynamic viscosity, γ is the air-liquid surface tension, g is the gravity acceleration, and R (≈ 5 cm) is the container radius. (b) Damping rate vs the amplitude of the angle measured at the container axis. ϕ^* indicates the value for which the contact line is pinned.

angles observed when the contact line is pinned (zero contact line speed), i.e., static hysteresis, has been ascribed to a solid-like friction exerted by the solid substrate on the fluid.^{14–16} According to the experiments,⁸ two different damping regimes can be observed, corresponding to higher and smaller oscillation amplitudes [see Fig. 1(b)]. (i) First, the contact line slides on the solid substrate experiencing progressive stick-slip transitions under the effect of the dynamic wall friction. In this phase, the damping increases considerably as the wave amplitude decreases, until it reaches a maximum value, after which it starts to decrease and the small amplitude regime is established. A final finite time of arrest for the contact line is found,¹⁶ so the interface pins, $\partial_t \eta = 0$ (pinned-end edge condition,^{17,18} where ∂_t is the time derivative), and (ii) the following pure bulk motion is seen to decay exponentially owing to the linear viscous dissipation acting in the fluid bulk and in the Stokes boundary layers at the solid bottom and sidewall.^{8,16}

Different theoretical frameworks, attempting to rationalize the nonlinear dependence of the damping rate on the oscillation amplitude, have been recently proposed.^{14,15} These works are based on an asymptotic formulation of the full hydrodynamic problem, which is tackled in the weakly nonlinear (WNL) and multiple timescale approach,¹⁹ under precise assumptions and range of validity. The

asymptotic analysis is found to be able to quantitatively predict the nonlinear trend of the damping in the higher amplitudes regime and the existence of a final finite time of arrest for the contact line, in agreement with experiments.^{8,16} However, it fails in capturing the transition to the smaller amplitudes regime, when the interface pins, but the fluid bulk keeps oscillating with a smaller amplitude motion following a pinned dynamics.

In vibration mechanics, a generalization of linear normal modes, the nonlinear normal mode expansion (NNMs) has been introduced (see Refs. 20–23 among many other references) for nonlinear dynamical systems as well as nonlinear continuous systems, by identifying the invariant manifolds governing the dynamics. The method was successfully applied to piecewise linear systems (see, for instance, Refs. 24 and 25).

The purpose of this paper is to provide a different theoretical approach, which overcomes the limitations of asymptotic analyses, thus successfully solving the overall flow dynamics, enabling us to extract and highlight realistic flow features. To this end, we consider viscous liquid oscillations in an idealized two-dimensional container and subjected to a realistic and experimentally inspired contact line model, to which the contact line is forced to obey. Using a piecewise time splitting of the nonlinear contact line law, we formalize a mathematical model based on successive projections between different sets of linear eigenmodes pertaining to each linear split-piece composing the contact line law. This procedure allows us to formally account for all the nonlinear features of small-amplitude capillary-gravity waves induced by a nonlinear contact line law acting at the lateral wall of a rectangular basin and, in particular, to correctly solve the transition from a the contact line stick-slip (or nearly stick-slip) regime to the pinned (or nearly pinned) one.

The manuscript is organized as follows. The flow configuration analyzed in this work and the physical model governing the problem are introduced in Sec. II. For completeness, the key points of the weakly nonlinear formulation applied to the present case are synthetically reposed and commented in Sec. III. The novel projection method is introduced and carefully described in Sec. IV, where quantitative and qualitative comparisons with the weakly nonlinear model and previous experiments are made. Last, the extension of the method to more sophisticated contact line dynamics is discussed in Sec. V. Final conclusions and comments are outlined in Sec. VI.

II. FLOW CONFIGURATION AND GOVERNING EQUATIONS

The viscous fluid motion within the two-dimensional vessel is governed by the incompressible Navier–Stokes equations,

$$\nabla \cdot \mathbf{u} = 0, \quad \partial_t \mathbf{u} + (\mathbf{u} \cdot \nabla) \mathbf{u} + \nabla p - Re^{-1} \Delta \mathbf{u} = -1 \hat{\mathbf{e}}_z, \quad (1)$$

which are made nondimensional by using the container's characteristic length l and the velocity \sqrt{gl} (see Fig. 2). Consequently, the Reynolds number is defined as $Re = \rho g^{1/2} l^{3/2} / \mu$ and the term $-1 \hat{\mathbf{e}}_z$ is the nondimensional gravity acceleration. At the free-surface $z = \eta$ kinematic and dynamic boundary conditions hold,

$$D(\eta - z)/Dt = \partial_t \eta + u \partial_x \eta - w = 0, \quad (2a)$$

$$[-p \mathbf{I} + Re^{-1} (\nabla \mathbf{u} + \nabla^T \mathbf{u}) - Bo^{-1} \kappa(\eta) \mathbf{I}] \cdot \mathbf{n} = \mathbf{0}, \quad (2b)$$

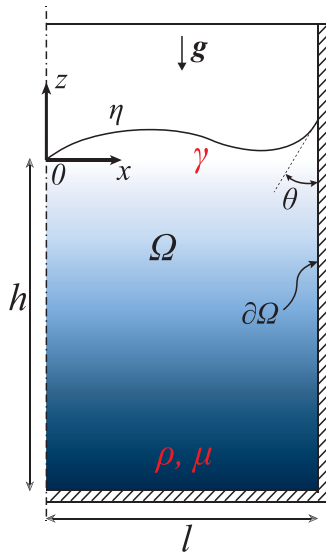


FIG. 2. Sketch of a two-dimensional rectangular container of width $2l$ and filled to a depth h (e.g., $h/l = 3$, nearly deep water regime, without loss of generality) with a liquid of density ρ and dynamic viscosity μ . The air-liquid surface tension is γ . The origin of the Cartesian coordinate system is fixed at the center of the free liquid surface at rest, while the bottom is placed at $z = -h$. θ is the contact angle. The dashed-dotted line is the geometrical axis of symmetry. Ω denotes the bulk domain, $\partial\Omega$ its solid boundaries, and η denotes here the moving interface.

where D/Dt is the material derivative, $\mathbf{u} = \{u, w\}^T$ is the velocity vector, $\kappa(\eta) = \partial_{xx}\eta(1 + \partial_x\eta^2)^{-3/2}$ is the free-surface curvature, and $\mathbf{n} = (1 + \partial_x\eta^2)^{-1/2} \{-\partial_x\eta, 1\}^T$ is the unit vector normal to the interface. The Bond number is defined as $Bo = \rho g l^2 / \gamma$, with γ designating the air-liquid surface tension. At the bottom wall, the no-slip condition applies,

$$\mathbf{u} = \{u, w\}^T = \mathbf{0} \quad \text{at } z = -h/l. \quad (3)$$

At the lateral walls, a slip length model is adopted, thus assuming that the fluid speed relative to the solid wall is proportional to the viscous stress^{26,27} and that, together with no-penetration condition, provides the boundary conditions

$$u = 0, \quad w + l_s \partial_x w = 0 \quad \text{at } x = \pm 1. \quad (4)$$

Such a condition is indeed needed in order to regularize the stress singularity at the moving contact line.^{28,29}

Last, at the contact line, $z = \eta$ and $x = \pm 1$, we include a phenomenological contact line law, which describes the nonlinear contact angle dynamic as a function of the contact line speed,

$$\partial_x \eta = \pm \cot \theta, \quad \theta - \theta_s = f(\partial_t \eta). \quad (5)$$

Relevant nonlinear laws, $f(\partial_t \eta)$, will be introduced in Sec. III.

It was hypothesized that a phenomenological macroscopic slip length appearing in Eq. (4) is not constant in space but rather a function of the position along the lateral wall and that it vanishes at a certain distance away from the contact line, where the flow obeys the no-slip condition.^{30,31} Furthermore, when the contact line motion is

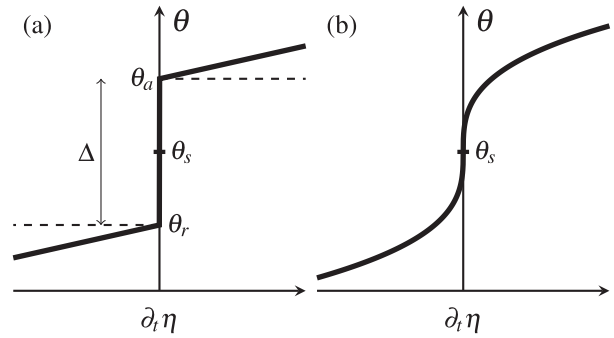


FIG. 3. (a) Hocking's¹⁰ linear law plus hysteresis range.^{9,33} (b) Jiang *et al.* cubic model,³² obtained in the framework of unidirectional flow over a flat plate at low Reynolds number.^{9,32}

modeled with a phenomenological law, which introduces a dependence on the contact line speed, e.g., Eq. (5), the value of the slip length at the contact line varies also in time and it is not arbitrary but rather linked to the prescribed contact line dynamics.^{30,31} However, in order to avoid the resulting dynamical coupling of the slip length l_s and the contact line motion, and since the dissipation at the wall in the contact line region (accounted for by the contact line model) dominates over that taken place at the lateral walls,¹⁰ we assume here a slip length $l_s \gg 1$, constant in time and space along the lateral wall, so that Eq. (4) for w reduces to a stress-free wall boundary condition. This simplistic assumption, which neglects the viscous boundary layer at the lateral walls, will result in an underestimation of the overall damping rate but it will significantly simplify the mathematical treatment of the lateral boundaries.

Finally, it is important to note that the simultaneous application of stress-free wall conditions and a pinned contact line does not result in any inconsistency,^{17,18} in marked contrast to the combination of no-slip wall conditions and a free-edge contact line.

Although a perfect slip condition is assumed at the lateral wall and albeit the overall dissipation is mainly ascribed to the nonlinear contact line dynamics, the role of the small linear viscous dissipation occurring in the fluid bulk and solid bottom is of crucial importance in avoiding the accumulation of energy in high frequencies in the forthcoming projection method, thus precluding the use of a simpler potential model.

Further details are given in Appendix C.

III. ASYMPTOTIC FORMULATION

The system of governing equations and boundary conditions introduced in Sec. II is nonlinear owing to the nonlinear contact angle law. Henceforth, we consider the following two experimentally based contact line laws from the literature^{8,9,32} (see Fig. 3):

$$\theta - \theta_s = \begin{cases} \alpha Ca \partial_t \eta + \Delta/2 \operatorname{sgn}(Ca \partial_t \eta), & \text{Hocking + hyst.,} \\ \beta Ca^{1/3} (\partial_t \eta)^{1/3}, & \text{Jiang et al.,} \end{cases} \quad (6)$$

with the capillary number defined as $Ca = \mu \sqrt{g l} / \gamma$.

To avoid misleading interpretations, we specify that in the following the terminology “Hocking’s law plus hysteresis” (or Hocking + hyst.) refers to a combination of the original Hocking’s linear law (without static hysteresis) supplemented with a static hysteresis range, Δ , as in Ref. 9.

Given the contact line nonlinearity, one possible approach to tackle the problem is asymptotic theory. In this section, we briefly repropose a weakly nonlinear (WNL) formulation, based on a multiple timescale expansion and valid in the limit of small contact line parameters, which aims to incorporate as much as possible, the features of the contact line dynamics.^{14,15} We draw the reader’s attention to the fact that the nomenclature adopted hereinafter relies on that used in the authors’ earlier works,^{14,15} the limitations of which motivated the present study.

A. Presentation

Let us introduce the following asymptotic expansion for the flow quantities:

$$\mathbf{q} = \{\mathbf{u}, p, \eta\}^T = \mathbf{q}_0 + \varepsilon \mathbf{q}_1 + \varepsilon^2 \mathbf{q}_2 + O(\varepsilon^3) \quad (7a)$$

(the same expansion holds for the contact angle θ). Under the assumption of small viscous effects ($Re \gg 1$) and introducing the following scalings for the slow time, damping coefficient, and contact line parameters:

$$\begin{aligned} \underbrace{T = \varepsilon t}_{\text{slow time scale}}, \quad \underbrace{\sigma_V = \varepsilon \hat{\sigma}_V}_{\text{viscous damping}}, \quad \underbrace{\Delta = \varepsilon^2 \hat{\Delta}}_{\text{nonlinear range}}, \\ \underbrace{\alpha Ca = \varepsilon \hat{\alpha}}_{\text{Hocking's linear variation}}, \quad \underbrace{\beta Ca^{1/3} = \varepsilon^{5/3} \hat{\beta}}_{\text{Jiang et al. cubic law}}, \end{aligned} \quad (7b)$$

with $\varepsilon \ll 1$ small parameter, the contact line nonlinearities are retained only as weakly nonlinear correction (order ε^2) of an ε -order dynamics representing an oscillatory small perturbation of the static flow configuration. Substituting the expansions above in the governing equations and boundary conditions, a series of systems are obtained at various orders in ε . We note that the small parameter ε is not explicitly defined here but rather it only serves to separate different order of magnitudes of the problem and it will be eliminated afterwards by recasting all quantities in terms of their corresponding physical values.^{14,15,34,35}

At order ε^0 , the nonlinear problem associated with the static shape of the interface is obtained. Although the procedure in principle applies to any static contact angle θ_s , we consider the simplest case $\theta_0 = \theta_s = \pi/2$ so that the fluid at rest ($\mathbf{u}_0 = \mathbf{0}$, $p_0 = -z$) has a flat static interface $\eta_0 = 0$. Note that the static contact angle θ_s represents the macroscopic contact angle measured with the fluid at rest before imposing any initial perturbation. At order ε , the linear eigenvalue problem for viscous capillary-gravity waves is retrieved. The contact line boundary condition reads $\partial_x \eta_1 = 0$ ($\theta_1 = 0$), thus retrieving the classic free-end edge condition. Assuming a single mode expansion, the marginally stable first order dynamics is described by Eq. (8),

$$\mathbf{q}_1(x, z, t) = A_1(T) \hat{\mathbf{q}}_1(x, z) e^{i\omega t} + c.c., \quad (8)$$

where $\hat{\mathbf{q}}_1(x, z)$ is a viscous free-end edge eigenmode (set by the initial condition) and ω is its corresponding eigenfrequency. We note that in a two-dimensional framework, the eigenmodes are represented by symmetric or anti-symmetric waves with respect to the container axis placed at $x = 0$. In the following, we arbitrarily consider the fundamental anti-symmetric (first or lowest oscillation frequency) mode, but the very same single mode analysis applies to any eigenfunction. We also note that the viscous damping coefficient of the eigenmode σ_V has been assumed of order ε and, therefore, only enters at next order. This assumption only serves to apply the formalism of the multiple scale analysis, which classically applies to marginally stable system.³⁶ As the Reynolds is typically high enough, the damping coefficient results in a slow damping process over fast wave oscillations and hence it can be directly englobed in the final amplitude equation. A possible way to account for such a first order departure from marginal stability is that discussed in Ref. 15. Another option, which leads to the same final results for this specific problem, but that is formally more general, is represented by the *shift operator* technique proposed in Ref. 34. Here, we opt for the second option. See Ref. 34 for a thorough discussion on this regard. A (T) is the mode amplitude, unknown at this stage, and allowed to vary on the slow time scale $T = \varepsilon t$. In the spirit of multiple scale expansion, the resonating effect of secular terms on the asymptotic solution is avoided at order ε^2 by imposing a compatibility condition, which prescribes an amplitude equation for A , slow amplitude modulation of the first order motion. The contact line dissipation enters at this order and, together with the viscous dissipation in the bulk, is incorporated in the structure of the amplitude equations (9) [according to the two contact line models introduced in Eq. (6)],

$$d_T A_1 + \hat{\sigma}_V A_1 = \begin{cases} -\hat{\zeta}_H A_1 - \hat{\chi}_H A_1 |A_1|^{-1}, & \text{Hocking + hyst.}, \\ -\hat{\chi}_J A_1 |A_1|^{-2/3}, & \text{Jiang et al.}, \end{cases} \quad (9)$$

with $\sigma_V = \varepsilon \hat{\sigma}_V$ the linear viscous damping coefficient, computed numerically as a solution of the ε -order eigenvalue problem. The r.h.s. of Eq. (9) clearly highlights the contact line terms contributing to the overall dissipation, namely, the ones proportional to $\hat{\zeta}_H$ and $\hat{\chi}_J$, which represent the dissipation induced by the linear (Hocking) or cubic (Jiang et al.) variation of the angle with the contact line speed, while the second term in Hocking’s model plus hysteresis range, $\hat{\chi}_H$, reproduces the dissipation associated with the contact angle hysteresis. Coefficients $\zeta_H = \varepsilon \hat{\zeta}_H$, $\chi_H = \varepsilon^2 \hat{\chi}_H$ read

$$\zeta_H = \frac{\lambda^2 \sin \theta_s \alpha C a \kappa}{Bo}, \quad \chi_H = \frac{\lambda^2 \sin \theta_s \Delta \kappa}{|\lambda| \pi Bo |\hat{\eta}_1|_{x=1}}. \quad (10)$$

with κ defined in Ref. 15 and with the complex eigenvalue $\lambda \approx i\omega$ as σ_V is of order ε . The expression of $\chi_J = \varepsilon^{5/3} \hat{\chi}_J$ is given in Appendix B of Ref. 15. For a thorough description of the weakly nonlinear formulation, the derivation of the amplitude equation coefficients and the numerical scheme used in this paper (based on a Chebyshev collocation method solved in Matlab), see Refs. 14 and 15. Henceforward, we will focus on the simpler Hocking’s model plus hysteresis.^{10,32} The more sophisticated extension of the projection approach proposed in Sec. IV to any nonlinear contact line function, including the Jiang et al. cubic model,³² will be discussed in Sec. V.

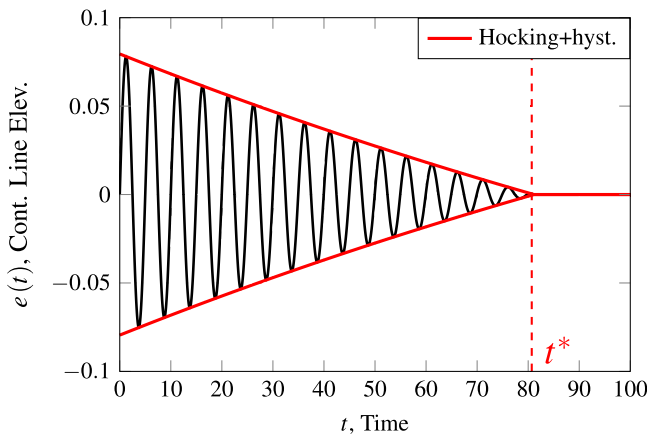


FIG. 4. Contact line elevation (black solid line), $e(t) = \eta|_{x=1}$, modulated by the slow time amplitude (red solid line) vs time and corresponding to the dominant (first) free-end edge anti-symmetric natural mode. We assumed pure water in a container of width $l = 5$ cm for which $Bo = 336$, $Re = 30\,717$, and $Ca = 0.011$. The chosen contact line parameters for Hocking's law are $\theta_s = \pi/2$ and $\alpha = 77$ rad with $\Delta = 20^\circ$. The initial contact line elevation and speed are set to 0 and 0.1, respectively. The initial absolute value and phase of the complex amplitude A , A_0 and Φ_0 , respectively, follows. t^* denotes the time of arrest (vertical red dashed line) prescribed by the WNL model.

B. Time of arrest and nonlinear damping

The amplitude A , obtained for Hocking's law plus hysteresis, is first calculated solving (9) (see Ref. 15) yielding (after eliminating ε by recasting each variable in terms of the corresponding total physical quantity, e.g., the physical time $t = T/\varepsilon$, the total amplitude $A = \varepsilon A_1$ and the initial condition $A_0 = \varepsilon a_0$)

$$|A(t)| = [A_0 + \chi_{Hr}/(\zeta_H + \sigma_V)] e^{-(\zeta_H + \sigma_V)t} - \chi_{Hr}/(\zeta_H + \sigma_V), \quad (11)$$

and then substituted in Eq. (8), which describes the time evolution of the first order dynamics, as displayed in Fig. 4 in terms of contact line elevation.

The associated damping rate can be then obtained as the logarithmic decrement of the amplitude $|A(t)|$ in time. However, we introduce here a different measure based on the gravitational potential energy density of the system, E_{pg} , which is, in general, a more suitable quantity to describe the overall system dynamics (and it will be used in Sec. IV). Since $E_{pg} = \int_{z=\eta_0} \eta^2 dx \sim |A|^2$, the damping rate is expressed as

$$\begin{aligned} DR_{E_{pg}} &= -d_t [\log(|A(t)|^2/A_0^2)] = -2|A(t)|^{-1} d_t |A(t)| \\ &= 2(\sigma_V + \zeta_{Hr}) + 2\chi_{Hr}/|A(t)| \end{aligned} \quad (12)$$

(the subscript t stands for the real part) and is presented in Fig. 5.

The value of the nondimensional oscillation frequency, ω , and the viscous damping coefficient, σ_V , corresponding to the dominant (first) antisymmetric wave with free-end edge contact line condition, plotted in Fig. 4, are, respectively, 1.258 and 1.16×10^{-4} , while the damping coefficient associated with Hocking's linear law is $\zeta_{Hr} = 4 \times 10^{-3}$, hence $(\sigma_V + \zeta_{Hr}) \approx \zeta_{Hr}$. The value of χ_{Hr} is 8.3×10^{-4} .

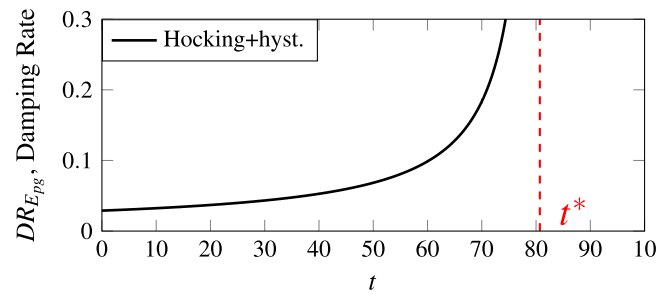


FIG. 5. Non-dimensional damping rate vs non-dimensional time, obtained for the same parameter setting of Fig. 4. The vertical lines indicate the time of arrest, t^* , for the contact line and, in this context, of the total motion.

C. Comments

The weakly nonlinear analysis reproposed^{14,15} in this section partially accounts for dissipative effects acting at the sliding contact line using asymptotic theory and reveals the strong influence of the nonlinear contact line dynamics on the damping of capillary-gravity waves in confined basins. Given that the linear viscous dissipation taking place in the fluid bulk and at the solid bottom, σ_V , is negligible compared to ζ_{Hr} , Eq. (12) suggests that there exist two main dissipation sources, a first one due to the linear contact angle variation with the contact line speed, ζ_{Hr} , and another due to hysteresis occurring at a zero speed, $\chi_{Hr}/|A(t)|$. The latter contribution depends on the sign of the contact line speed only and, therefore, it may be interpreted as a Coulomb-like friction force, responsible for the predominantly linear decay and thus for the arrest of the motion at finite time. In fact, the damping rate is found to depend on the initial condition and on the wave amplitude variation in time.^{6,8,14-16} More precisely, as the amplitude decreases, the damping rate increases and eventually diverges in finite time leading to the finite time arrest of the contact line (see Fig. 5) for $|A(t=t^*)| = 0$. Nevertheless, the weakly nonlinear theory fails in capturing the transition to the smaller amplitude regime observed in Refs. 8 and 16, when the contact line is pinned and the fluid bulk keeps oscillating with a pinned-end edge dynamics. This limitation is intrinsic to the asymptotic formulation, which only predicts the evolution of the amplitude of a leading order free-end edge mode. Consequently, it prescribes the arrest of the total fluid motion once the contact line is pinned at $t = t^*$, thus overlooking the remaining bulk oscillations submitted to a finite, and small, damping rate. Furthermore, even during the initial higher amplitude sloshing motion, the contact line exhibits periodic stick-slip transitions, which is not captured with a weakly nonlinear approach. In other words, the asymptotic model neglects the slowing increasing fraction of the time period during which the contact angle changes while the contact line is at rest (pinned fraction of liquid motion).

IV. PROJECTION METHOD

In Sec. III, we brought to light the main limitations of the weakly nonlinear analysis, which, by construction, introduces the contact line dissipation only at higher order and is unable to capture

the slip-sticking regime observed in the experiments. In this section, we propose and formalize a different mathematical approach based on a sequential eigenfunction projection aiming at overcoming these limitations and at providing a more complete and realistic characterization of the liquid motion. To this end, we first introduce here the projection method in its simplest formulation considering as contact line boundary condition Hocking's model plus hysteresis of Fig. 3(a), with the angle varying linearly for a non-zero contact line speed. Subsequently, the projection approach is compared with the asymptotic model. The results of the analysis are then discussed in light of previous laboratory experiments⁸ (in a cylindrical container) before generalizing the method to solve the nonlinear Jiang *et al.* law in Sec. V.

A. Application to Hocking's law plus hysteresis

1. Formalism

In contradistinction with the weakly nonlinear approach where the nonlinearities enter at second order, the contact line model is accounted for at first order, thus solving a nonlinear problem. In practice, the total flow field is expanded as

$$\mathbf{q}_{tot} = \mathbf{q}_0 + \varepsilon \mathbf{q} + \mathcal{O}(\varepsilon^2), \quad (13)$$

with the rest state $\mathbf{q}_0 = \{\mathbf{u}_0 = \mathbf{0}, p_0 = -z, \eta_0 = 0\}^T$, $\theta_0 = \theta_s = \pi/2$, and with the only assumption of small hysteresis of order ε , i.e., $\Delta = \varepsilon \hat{\Delta}$. Note that the viscous damping coefficient is not required to be small. In this limit of small perturbation, the only nonlinearity appearing in the system is attributed to the contact line dynamics through the geometrical relation (5). When the contact line motion is schematized using Hocking's law plus hysteresis range, we can identify two well-distinct phases of the dynamics, one in which the angle varies linearly with a slope α as a function of the contact line speed (Hocking's linear law) and one in which the contact line is pinned at a certain elevation and with zero velocity (static hysteresis). We denote these two phases as free and pinned phase, respectively. Hence, we can write two different boundary conditions associated with the two phases (e.g., at the contact line, $z = 0$, $x = 1$),

$$\underbrace{\partial_x \eta_f|_{x=1} + \alpha Ca \partial_t \eta_f|_{x=1}}_{\text{free-phase l.h.s.}} = \underbrace{-\theta^\pm}_{\text{free-phase r.h.s.}}, \quad (14)$$

$$\partial_t \eta_p|_{x=1} = 0 \longrightarrow \underbrace{\eta_p|_{x=1}}_{\text{pinned-phase l.h.s.}} = \underbrace{\text{const.}}_{\text{pinned-phase r.h.s.}}, \quad (15)$$

where subscripts f and p stand for free-phase and pinned-phase, respectively, and $\theta^\pm = \pm \hat{\Delta}/2$ for a symmetric hysteresis range centered around θ_s . In other words, the free-phase has a non-homogeneous Robin boundary condition at the contact line, while the pinned-phase has a non-homogeneous Dirichlet condition. In both phases, the solution is thus rewritten as the sum of a homogeneous solution (generalized eigenvalue problem) and a static ($\partial_t \eta = 0$, $\mathbf{u} = \mathbf{0}$) particular solution, which must satisfy the following

static equation (linearized meniscus equation) and boundary conditions,

$$\eta_{fs} - Bo^{-1} \partial_{xx} \eta_{fs} = p_{fs} = \text{const.}, \quad \text{with } \partial_x \eta_{fs}|_{x=1} = -1, \quad (16)$$

$$\eta_{ps} = \eta_{fs}/F_0, \quad \text{with } F_0 = \eta_{fs}|_{x=1}, \quad (17)$$

where s denotes the static particular solution, $\partial_{xx} \eta$ represents the ε -order curvature operator, linearized around $\eta_0 = 0$ for the present case with $\theta_s = \pi/2$ [owing to the expansion (13)] and the minus sign in Eqs. (14) and (16) comes from the linearization of $\cot \theta$ in Eq. (5) at $x = 1$. The constant on the r.h.s. of Eq. (16) [different from that of Eq. (15)], which is trivially zero for an anti-symmetric wave dynamics, is instead computed by imposing the mass conservation constraint, $\int_{z=\eta_0} \eta_{fs} dx = 0$, when the symmetric dynamics is considered. For convenience of notation, instead of imposing $-\theta^\pm$ in the r.h.s. of the boundary condition to Eq. (16) at $x = 1$, we impose -1 , and we kept θ^\pm explicit in front of \mathbf{q}_f , state vector of the particular solution associated with the free-phase. \mathbf{q}_p is its analogous in the pinned-phase. The two particular solutions, \mathbf{q}_f and \mathbf{q}_p , up to their associated constant, θ^\pm and e_{fp} , are displayed in Figs. 6(a) and 6(b). The solution in the two phases is thus expressed as follows:

$$\mathbf{q}_f = \theta^\pm \mathbf{q}_f + \left(\sum_{n=1}^{N_f} A_{fn} \hat{\mathbf{q}}_{fn} e^{\lambda_{fn}(t-T_f)} + c.c. \right), \quad (18a)$$

$$\mathbf{q}_p = e_{fp} \mathbf{q}_p + \left(\sum_{m=1}^{N_p} B_{pm} \hat{\mathbf{q}}_{pm} e^{\lambda_{pm}(t-T_p)} + c.c. \right), \quad (18b)$$

where N_f and N_p are the truncation numbers of the series representing the homogeneous solutions, $\hat{\mathbf{q}}_{fn}$, $\hat{\mathbf{q}}_{pm}$ and λ_{fn} , λ_{pm} are the eigenmodes and eigenvalues obtained solving numerically the corresponding generalized eigenvalue problem [see Figs. 6(c)–6(j)], and A_{fn} and B_{pm} are the complex amplitude coefficients associated with each mode. Without loss of generality, we consider $N_f = N_p = N$ in the following. Importantly, during this pinned-phase, the nonzero static solution [see Eq. (17)] allows the interface to transiently oscillate with a contact line elevation fixed to the value assumed at the transition from the previous free-phase to the next pinned-phase, e_{fp} . Figure 6 gathers all the ingredients needed to formalize the projection scheme and we can now proceed in the description of its practical application to temporal flow evolution. A convergence analysis for a test case of eigenvalue calculation is given in Appendix A.

2. Temporal evolution description

Let us initialize the dynamics starting from the free-phase (advancing, θ^+ or receding, θ^- , path) assigning arbitrary values to the complex amplitudes $A_{fn} = A_{fn}^0$ for $t = T_f = 0$. The system will then evolve following the dynamics described by Eq. (18a). By virtue of the mode normalization introduced in Figs. 6(c)–6(f), for which $\eta_{fn}|_{x=1} = 1$ and $\eta_{fs}|_{x=1} = F_0$, the contact line elevation, $\eta|_{x=1} = e$,

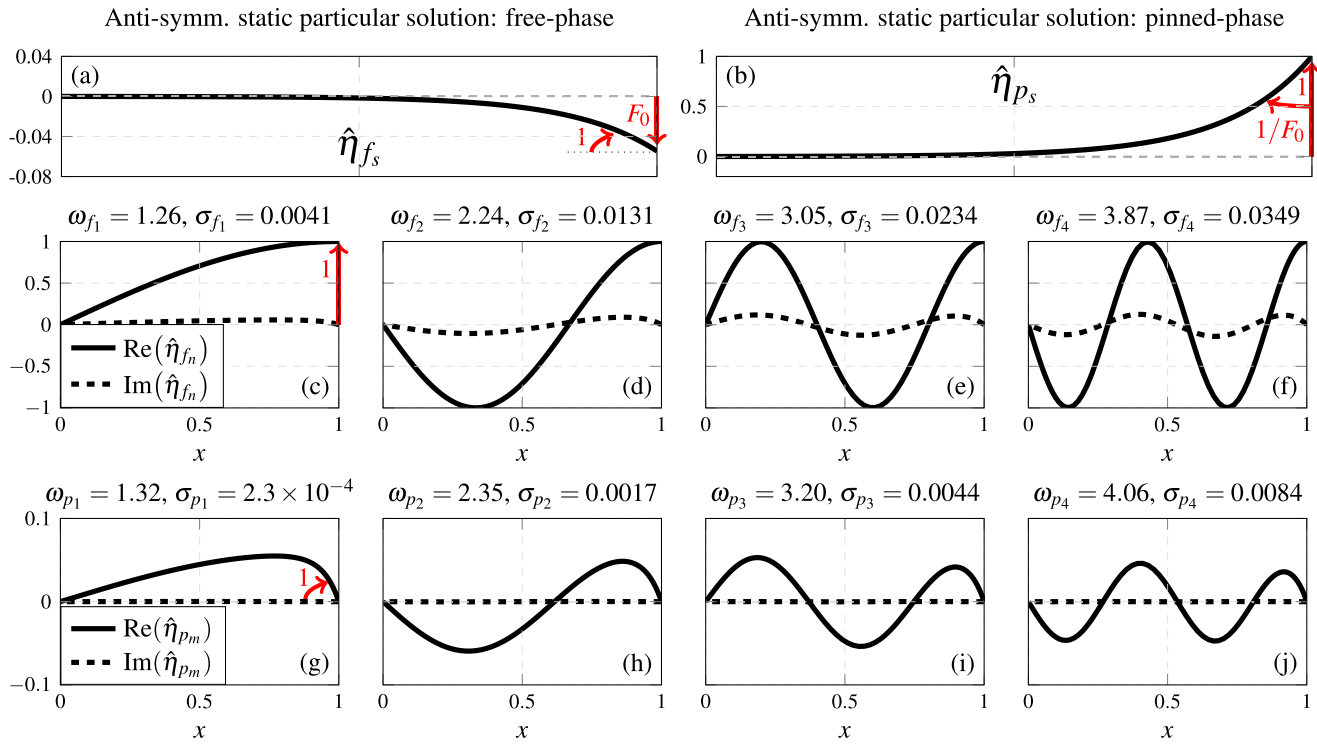


FIG. 6. (a) and (b) Static particular solutions for the anti-symmetric free and pinned dynamics, respectively. Note that the radial values of the two particular solutions are plotted up to their corresponding constants, θ^\pm and e_{fp} , respectively, which will be determined by the time-marching of the projection algorithm. (c)–(f) Eigensurface associated with the first four anti-symmetric modes corresponding to the free-dynamics. Only half domain, $x \in [0, 1]$, is shown. The modes are normalized with the phase of the interface at the contact line and its absolute value so that the contact line elevation is 1. (g)–(j) Eigensurface associated with the first four anti-symmetric modes corresponding to the pinned dynamics. The modes are normalized with the phase of the interface at the contact line and its slope so that the slope in $x = 1$ is 1. As in Fig. 4, we assumed pure water in a container of width $l = 5$ cm for which $Bo = 336$, $Re = 30\,717$, and $Ca = 0.011$. The static angle is $\theta_s = \pi/2$ and the slope α is set to 77 rad. The linear eigenfrequency and damping associated with each mode are denoted by ω and σ , respectively. Note that, despite the lower frequencies, the damping associated with the free-modes, which englobe part of the contact line dissipation due to the linear variation of the angle (Hocking's linear law), is higher than the one for pinned modes, where only the viscous bulk dissipation is present (we recall that the viscous boundary layers at the lateral walls are neglected by imposing a stress-free condition; see also the [supplementary material](#)).

and speed, $\partial_t \eta|_{x=1} = \dot{e}$, in this phase read

$$e = \theta^\pm F_0 + \left(\sum_{n=1}^N A_{fn} e^{\lambda_{fn}(t-T_f)} + c.c. \right), \quad (19a)$$

$$\dot{e} = \left(\sum_{n=1}^N \lambda_{fn} A_{fn} e^{\lambda_{fn}(t-T_f)} + c.c. \right). \quad (19b)$$

The second equation (19b) provides a criterion for the transition to the pinned-phase. Indeed, letting evolving in time equation (19b) until $\dot{e} = 0$, we can compute the time T_p at which the transition from the free-phase to the pinned-phase occurs. At the transition, $t = T_p$, the physical condition is the continuity of the whole set of flow quantities, $\mathbf{q}_f(t = T_p) = \mathbf{q}_p(t = T_p)$, which translates into the following

equivalence:

$$\begin{aligned} e_{fp} \mathbf{q}_{ps} + \left(\sum_{m=1}^N B_{pm} \hat{\mathbf{q}}_{pm} + c.c. \right) \\ = \theta^\pm \mathbf{q}_s + \left(\sum_{n=1}^N A_{fn} \hat{\mathbf{q}}_{fn} e^{\lambda_{fn} \Delta T_{fp}} + c.c. \right), \end{aligned} \quad (20)$$

with $\Delta T_{fp} = T_p - T_f$. Noting that the contact line elevation at the transition time is

$$e_{fp} = \theta^\pm F_0 + \left(\sum_{n=1}^N A_{fn} e^{\lambda_{fn} \Delta T_{fp}} + c.c. \right), \quad (21)$$

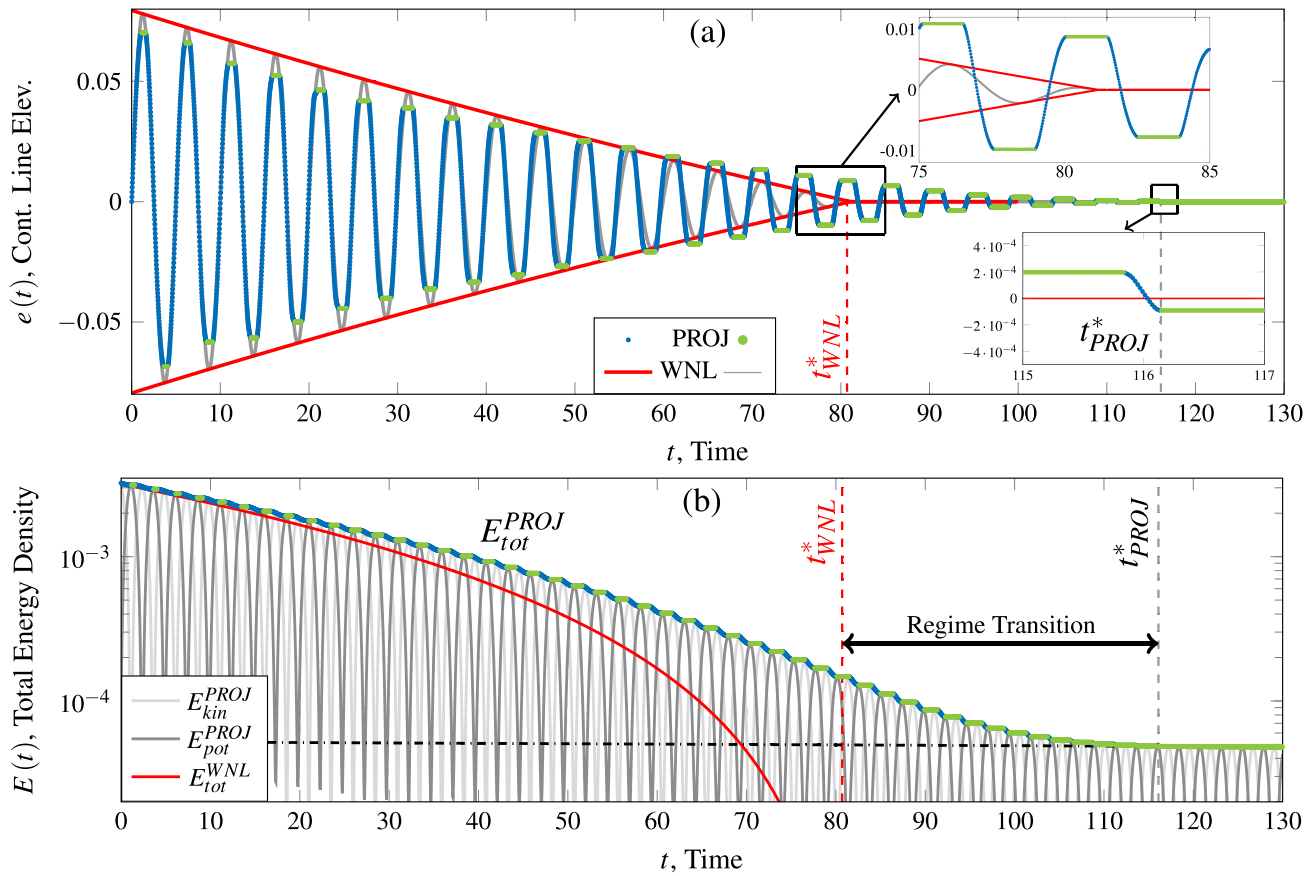


FIG. 7. (a) Contact line elevation vs time. The blue and green colors indicate the free and pinned phases, respectively. Parameters are set as in Fig. 4, with a static hysteresis range $\Delta = 20^\circ$. We initialize the problem setting the complex amplitude of the first antisymmetric mode in order to have an initial contact line elevation and speed equal to 0 and 0.1, respectively. t_{WNL}^* and t_{PROJ}^* denote the final time of arrest for the contact line resulting from the weakly nonlinear calculation (WNL) and from the projection scheme (PROJ). (b) Different contributions to the instantaneous total energy of the system (log scale) vs time (linear scale). Only the total energy is displayed (red solid line) for the WNL model. The black dashed-dotted line represents the final exponential decaying following the pinning of the contact line. The series associated to each phase are truncated to $N = 30$. The time step used to advance the algorithm in time was set to $\Delta t = 0.005$. The filled circles in (a) correspond to a sampling period of 0.05. See also Integral Multimedia Movie 1 for a full free-surface dynamic representation. Multimedia view: <https://doi.org/10.1063/5.0055898.1>

and $\mathbf{q}_{fs} = F_0 \mathbf{q}_{ps}$, Eq. (20) is rewritten as

$$\sum_{m=1}^N B_{pm} \hat{\mathbf{q}}_{pm} + c.c. = \underbrace{\sum_{n=1}^N A_{fn} (\hat{\mathbf{q}}_{fn} - \mathbf{q}_{ps}) e^{\lambda_{fn} \Delta T_{fp}}}_{\mathbf{f}_{fp}} + c.c., \quad (22)$$

where the pinned static particular solution is subtracted from the r.h.s. In other words, once the particular solution is subtracted from the r.h.s., the field \mathbf{f}_{fp} satisfies the boundary conditions of the linear problem for the pinned-phase; therefore, \mathbf{f}_{fp} can be represented as a linear combination of modes pertaining to the pinned-phase. The unknown amplitudes B_{pm} are thus obtained applying a projection step. To this end, let us introduce the following weighted scalar

product,

$$\langle \mathbf{w}, \mathbf{v} \rangle_E = \int_{\Omega} \bar{\mathbf{u}}_{\mathbf{w}} \mathbf{u}_{\mathbf{v}} d\Omega + \int_{z=0} (\bar{\eta}_{\mathbf{w}} \eta_{\mathbf{v}} + Bo^{-1} \partial_x \bar{\eta}_{\mathbf{w}} \partial_x \eta_{\mathbf{v}}) dx, \quad (23)$$

where $\mathbf{v} = \{\mathbf{u}_{\mathbf{v}}, p_{\mathbf{v}}, \eta_{\mathbf{v}}\}^T$ and $\mathbf{w} = \{\mathbf{u}_{\mathbf{w}}, p_{\mathbf{w}}, \eta_{\mathbf{w}}\}^T$ are two generic vectors, the bar designates the complex conjugate, Ω denotes the fluid bulk domain ($d\Omega = dx dz$), and the subscript E stands for energy. It follows that the energy norm of a generic vector \mathbf{v} is given by

$$\langle \mathbf{v}, \mathbf{v} \rangle_E = ||\mathbf{v}||_E^2 = \underbrace{\int_{\Omega} \bar{\mathbf{u}}_{\mathbf{v}} \mathbf{u}_{\mathbf{v}} d\Omega}_{\sim E_k^v} + \underbrace{\int_{z=0} \bar{\eta}_{\mathbf{v}} \eta_{\mathbf{v}} dx}_{\sim E_{pg}^v} + Bo^{-1} \underbrace{\int_{z=0} \partial_x \bar{\eta}_{\mathbf{v}} \partial_x \eta_{\mathbf{v}} dx}_{\sim E_{ps}^v}. \quad (24)$$

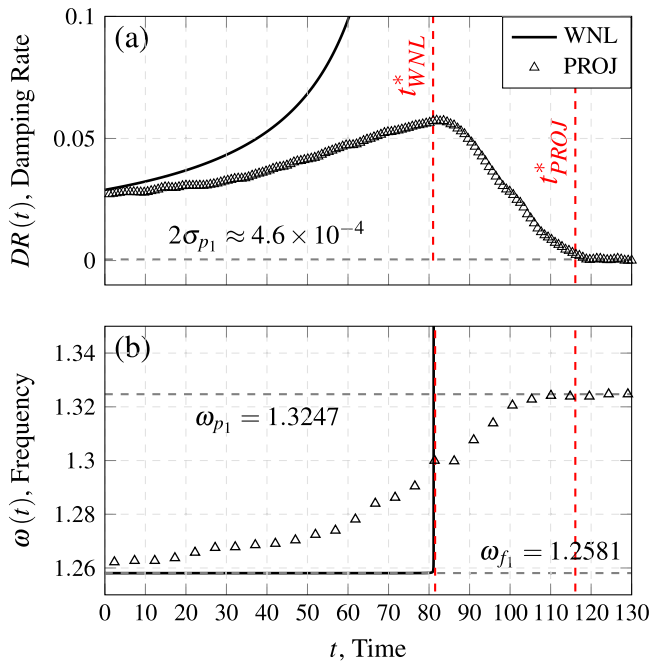


FIG. 8. (a) Nondimensional damping rate and (b) frequency modulation vs time. The damping rate is computed as the logarithmic decrement of the potential energy amplitude, shown in Fig. 7. The frequency is computed from the potential energy evaluating the period from peak to peak and the resulting value [triangle in (b)] is then roughly assigned to the midpoint of the corresponding time interval.

One can recognize that the three integrals in Eq. (23) represent a measure of the total energy density, given by the sum of kinetic, gravitational potential, and surface potential energy densities, respectively, stored in \mathbf{v} . Invoking the concept of adjoint modes, solutions of the adjoint linearized problem, it can be demonstrated that the direct modes, $\hat{\mathbf{q}}_i$, and the adjoint modes, $\hat{\mathbf{q}}_i^\dagger$, form a bi-orthogonal basis with respect to the scalar product (23). Moreover, the adjoint modes can be normalized such that $(\hat{\mathbf{q}}_i^\dagger, \hat{\mathbf{q}}_j)_E = \delta_{ij}$, with δ_{ij} being the Kronecker delta. Further insights about the derivation of the adjoint problem and the demonstration of the bi-orthogonality condition with respect to (23) are given in the [supplementary material](#).

Hence, we can project the known vector \mathbf{f}_{pf} onto the pinned basis and the amplitude coefficients B_{pm} are obtained as

$$B_{pm} = (\hat{\mathbf{q}}_{pm}^\dagger, \mathbf{f}_{pf})_E. \quad (25)$$

where $\hat{\mathbf{q}}_{pm}^\dagger$ is the adjoint mode that is bi-orthogonal to the direct mode basis, which is made of pairs of complex conjugate eigenvectors, $\hat{\mathbf{q}}_{pm}$ and $\hat{\mathbf{q}}_{pm}^*$, associated with pairs of complex conjugate eigenvalues, λ_{pm} and $\bar{\lambda}_{pm}$ (see also the [supplementary material](#)).

At this point, the system is in the pinned-phase and its time evolution is described by Eq. (18b). The contact line elevation is fixed to e_{fp} and contact angle varies within the prescribed hysteresis range. Given the eigenmode normalization used for η_{pm} [see

Figs. 6(g)–6(j)], the contact angle variation can be expressed as

$$\theta = e_{fp}/F_0 + \left(\sum_{m=1}^N B_{pm} e^{\lambda_{pm}(t-T_p)} + c.c. \right). \quad (26)$$

The transition to the next free-phase will occur at $t = T_f$, when $\theta = \theta^\mp$ (the sign depends on the semicycle considered) so that

$$\sum_{n=1}^N A_{fn} \hat{\mathbf{q}}_{fn} + c.c. = \underbrace{\sum_{m=1}^N B_{pm} (\hat{\mathbf{q}}_{pm} - \mathbf{q}_f)}_{\mathbf{f}_{pf}} e^{\lambda_{pm} \Delta T_{pf}} + c.c. \quad (27)$$

Analogously to (25), we now project the known vector \mathbf{f}_{pf} onto the free-basis, obtaining

$$A_{fn} = (\hat{\mathbf{q}}_{fn}^\dagger, \mathbf{f}_{pf})_E. \quad (28)$$

Essentially, we let the system evolve in time applying a projection step at each transition. During the evolution, the system dissipates energy and eventually, after a certain number of cycles, it gets trapped in the pinned-phase, the contact line arrests and the fluid motion decays exponentially to its equilibrium state under the effect of the viscous bulk dissipation only.

B. Results and discussion

In this section, the relevant results are discussed. In Fig. 7(a) (Multimedia view) the contact line elevation is plotted vs time. First, we observe that the actual final time of arrest for the contact line is higher than the one predicted by the weakly nonlinear model. Furthermore, the projection scheme is able to describe the transient stick-slip contact line motion. Indeed, the blue and green colors correspond to the time spent by the contact line in the free-phase and pinned-phase, respectively. During the dynamics, the contact line slides over the solid substrate, subjected to dynamic friction (linear contact angle variation in the free-phase), and transiently sticks when it reaches zero speed (hysteresis range), until the bulk inertia dominates again over the static friction and the triple line de-pins.

As shown in Fig. 7(b), during the motion, the system dissipates energy, consequently the time spent in the pinned-phase becomes larger and larger and eventually the inertia is not enough to overcome the static friction. The final pinned dynamics is, therefore, established at $t = t_{PROJ}^*$. As the lower inset in Fig. 7(a) reveals, the contact line does not arrest at the zero equilibrium position but rather at a turning position (compatible with the prescribed hysteresis range), i.e., $e(t = t_{PROJ}^*) \neq 0$, $\theta(t = t_{PROJ}^*) \neq \theta_s$, thus meaning that some little potential energy will be still present in the system at the end of the dynamics, in analogy with dynamical systems subjected to dry friction.

One of the main limitation of the weakly nonlinear model is enlightened in Fig. 7(b). Although the asymptotic analysis captures the initial nonlinear decaying trend of total energy density (due to dynamic and static contact line friction), computed as

$$E_{tot}^{t_i} = \int_{\Omega} \mathbf{u}_{t_i}^2 d\Omega + \int_{z=\eta_0} \left[\eta_{t_i}^2 + Bo^{-1} (\partial_x \eta_{t_i})^2 \right] dx \quad (29)$$

(t_i designates the i th time instant), it predicts the total arrest of the motion at $t = t_{WNL}^*$ and thus it fails in capturing the transition to

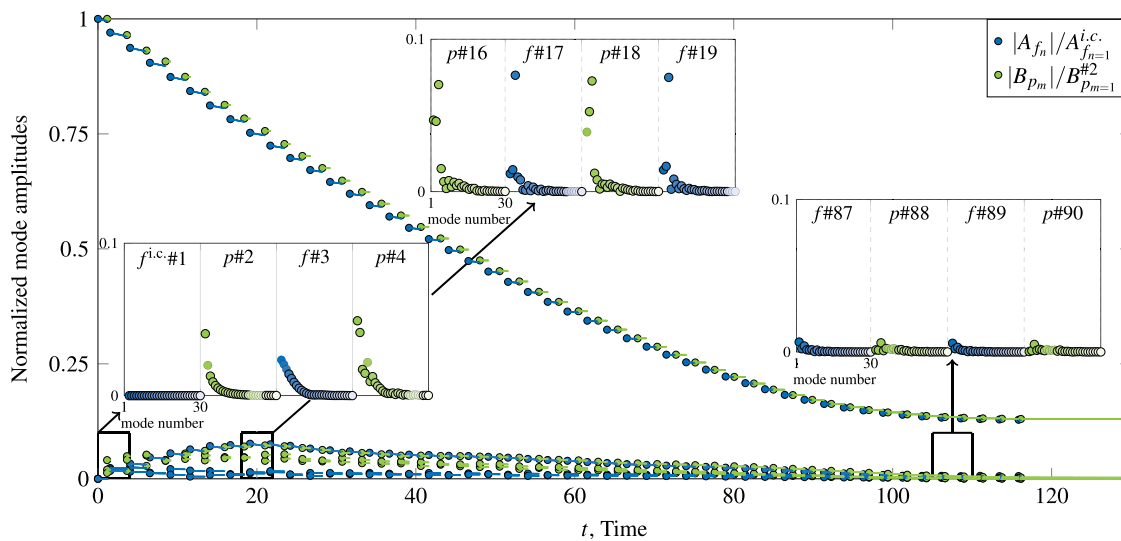


FIG. 9. Main figure: first four mode amplitudes vs time and corresponding to the case of Fig. 7. The free-phase amplitudes are normalized in this plot with the initial condition (only $A_{f_{n=1}} \neq 0$), while the pinned-phase amplitude is rescaled with the value of $B_{p_{m=1}}$ computed at the first projection from the free-phase to the pinned-phase. The colors are chosen in agreement with Fig. 7(a). Filled circles represent the amplitude values at the transition instant, while solid lines give their temporal evolutions according to their decay rates. The total $N = 30$ amplitudes, computed at each projection time, $t = T_f$ (blue) and T_p (green), are shown in the insets for different projection steps.

the final pinned dynamics, where the fluid bulk keeps oscillating with smaller amplitudes and with a fixed contact line elevation. As a consequence, the total energy in this final state is not zero yet but rather decays exponentially due to viscous bulk dissipation [linear trend in Fig. 7(b) for $t > t_{PROJ}^*$, black dashed-dotted line], as correctly captured by the projection method.

As time progresses, note that the fraction of time spent in the pinned-phase (in green) increases while the time spent in the free-phase (in blue) decreases, resulting in a slow modulation of the instantaneous damping rate and instantaneous frequency (see Fig. 8), as also observed in experiments.⁸ In particular, in the higher amplitude regime, the damping rate increases as the wave amplitude decreases and until reaching a maximum value, after which it decreases to a nearly constant value. Interestingly, despite the lack of quantitative accuracy of the weakly nonlinear calculation, the predicted time of arrest t_{WNL}^* seems to coincide with the maximum of the damping rate. Indeed, the time $t = t_{WNL}^*$, when the contact line is still oscillating, but with smaller amplitude, approximately predicts the beginning of the transition to the final pinned state, which will become fully established only at $t = t_{PROJ}^*$.

Once the pinned dynamic lasts the whole oscillating period, the damping rate is approximately constant and equal to the viscous damping coefficient of the first antisymmetric pinned mode [see Fig. 6(g)]. Concerning the frequency modulation in time, the weakly nonlinear theory gives an incorrect behavior, with an abrupt and nonphysical increase at $t = t_{WNL}^*$, corresponding to the finite time singularity. On the contrary, the projection scheme enables us to describe a smooth saturation from the characteristic value of the first antisymmetric free-mode, used to initialize the dynamics, to a final value, reached at $t = t_{PROJ}^*$ and

corresponding to the natural oscillation frequency of the first pinned-mode.

Last, Fig. 9 provides a deeper insight on how the projection procedure works, showing the normalized mode amplitudes in the case reported in Fig. 7, with the series (18a) and (18b) truncated at

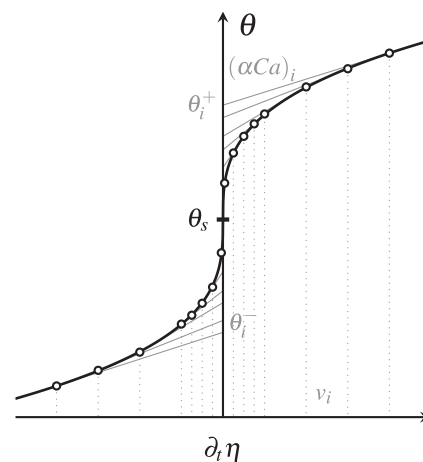


FIG. 10. Reduction of the Jiang *et al.* cubic model to a piecewise linear function via discretization of the cubic law in a set of linear steps with a given slope, $(\alpha Ca)_i$ and intercept θ_i^\pm . The discretization introduce a series of transition conditions between two consecutive free-phases at different contact line speeds, δ_i . A nonuniform discretization better approximates the transition to the pinned-phase at small velocity.

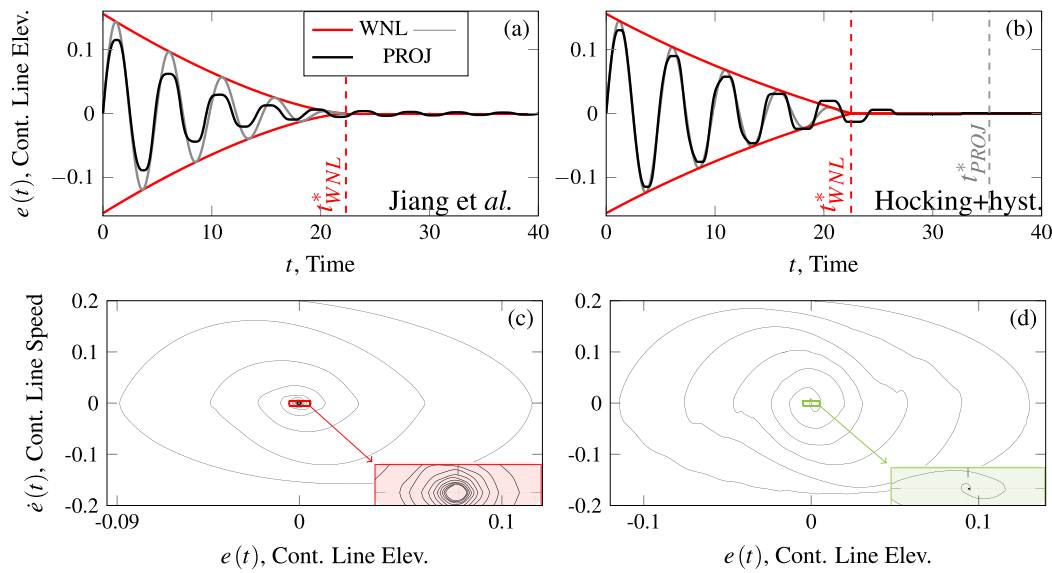


FIG. 11. (a) Contact line elevation vs time for pure water in a container of width $l = 1.93$ cm for which $Bo = 50$, $Re = 7367$, and $Ca = 0.0068$. The contact line parameters for the Jiang *et al.* law are $\theta_s = \pi/2$ and $\beta = 5.3$. We initialize the problem setting the complex amplitude of the first antisymmetric mode in order to have an initial contact line elevation and speed equal to 0 and 0.2, respectively. Red and gray solid lines: weakly nonlinear model (WNL). Black solid line: projection scheme (PROJ). t_{WNL}^* denotes the time of arrest computed solving amplitude Eq. (9) for the Jiang *et al.* model (see Ref. 15). (c) Phase portrait: contact line velocity vs contact line elevation from PROJ. The results are obtained discretizing the contact angle law in 61 sublinear pieces (30 equispaced steps in $|\partial_t \eta|_{x=1} \in [0.01, 0.2]$ and 31 in $\in [0, 0.01]$), requiring the solution of 31 eigenvalue problem (the law is symmetric). The series are truncated to $N = 10$ modes. The time evolutions were stopped at $t = 50$ with a time step $\Delta t = 0.005$. See also Appendix B and Integral Multimedia Movie 3 for a full free-surface dynamic representation and comparison with semi-linear direct numerical simulation (Multimedia view). (b) and (d) same as (a) and (c) with the contact line parameters for Hocking's law with hysteresis $\theta_s = \pi/2$, $\alpha = 123$ rad, and $\Delta = 18.5^\circ$. The series are truncated to $N = 30$ modes. See also Integral Multimedia Movie 2 for full free-surface dynamic representation. Multimedia view: <https://doi.org/10.1063/5.0055898.2>; <https://doi.org/10.1063/5.0055898.3>

$N = 30$ and starting, as initial condition, from a nonzero amplitude of the first antisymmetric free-mode only, i.e., $A_{f_{n=1}}^{i.c.}$. It follows that all the other mode amplitudes, A_{f_n} , are initially zero, as visible in the inset in the bottom-left corner of Fig. 7 ($f_{i.c.}^{\#1}$, where the superscript $i.c.$ stands for initial condition). At the first transition, mode $f_{n=1}$ is projected onto the pinned eigenmode basis ($p_{m=1}$), thereby exciting a certain number of pinned modes. In practice, at each projection, the system total energy is transferred from an eigenvalue basis to the other and it is partitioned among the various modes. In the case of Fig. 9, given the prescribed initial state, the total energy is mainly exchanged between the two corresponding modes ($f_{n=1}$ and $p_{m=1}$), with usually no more than 15 modes being excited, most of them having a negligible small amplitude and contributing only weakly to the overall dynamics. Given the prescribed initial condition, most of the energy is indeed contained in the first free-mode and in the corresponding pinned-mode.

A careful convergence and error analysis in relation to the truncation number of the series, N , is provided in the [supplementary material](#).

V. EXTENSION TO THE FULLY NONLINEAR JIANG ET AL. MODEL

The formalism of the projection scheme presented in Sec. IV A for Hocking's contact line model with hysteresis range is based on

the possibility to decompose the contact line law as the sequence of two (non-homogeneous) linear problems satisfied in each phase by the sum of a linear homogeneous solution and a particular static solution. For this reason, the extension to a fully nonlinear law, e.g., Jiang *et al.* cubic model³² may look challenging. Nevertheless, the continuous nonlinear law, e.g., cubic, can be split through a piecewise linear function (see Fig. 10) for which the projection approach is applicable.

In other words, the contact line law is split in a user-defined number of linear sub-phases having an equivalent Hocking's slope $(\alpha Ca)_i$, in which the system can be still represented as a homogeneous (solution of the corresponding i th generalized eigenvalue problem) plus a particular static solution,

$$\mathbf{q}^i = \theta_i^\pm \mathbf{q}_s^i + \left(\sum_{n=1}^N C_n^i \hat{\mathbf{q}}_n^i e^{\lambda_n^i (t-T^i)} + c.c. \right). \quad (30)$$

As the contact line dynamics is advanced in time, a series of transitions occur when the contact line speed is $\dot{e}_i = v_i$ (see Fig. 10), and the i th phase solution is progressively projected from one set of eigenmodes to next one ($i + 1$ -th), following the prescribed contact line law. As the system dissipates energy during the motion, it will eventually end in the central nearly pinned-phase (zero equilibrium point, $\theta = \theta_s$, $\eta(x) = \eta_0$, $\partial_t \eta|_{x=1} = 0$) where the motion decays exponentially owing to the viscous dissipation solely.

In contrast with Hocking's model with hysteresis, where only two phases are defined, here one has to solve numerically a certain number of eigenvalue problems, one for each sub-phase (see Fig. 10), thus yielding to a computationally more expensive calculation. However, the smooth cubic contact line law facilitates the projection algorithm, i.e., at each projection, the energy is transferred only among few modes, allowing one to truncate the modal series to a lower number of natural modes. The competition of a higher number of modes (excited at each projection) in the case of Hocking's law with hysteresis, when compared to the smooth cubic law, is visible in Figs. 11(a) and 11(c) (smoother time series) (Multimedia view) and Figs. 11(b) and 11(d) (shakier time series) (Multimedia view).

Figures 11(a) and 11(b) show the contact line elevation and speed computed via the projection method and weakly nonlinear model (see Ref. 15) for Jing and Perlin's cubic law.

From a mathematical and physical perspective, the main difference introduced by Jiang *et al.* law with respect to Hocking's law with hysteresis is the nature of the nonlinearity at zero contact line speed. The strong nonlinearity occurring at $\partial_t \eta|_{x=1} = 0$ introduces in the contact line motion a sort of solid-like friction effect at higher amplitudes (most active in the initial dynamics), which provokes the initial circular-pieces-like behavior in the phase portrait displayed in Fig. 11(c). However, in this case, there exists only one possible final equilibrium state with $e(t)|_{t \rightarrow +\infty} = 0$ and $\theta(t)|_{t \rightarrow +\infty} = \theta_s$, to which the system will tend asymptotically owing to the little viscous bulk dissipation. It follows that the contact line elevation and velocity are never exactly zero and, therefore, the phase portrait progressively turns into a classic logarithmic spiral, typical of linearly damped mechanical systems. Again, the limitations of the weakly nonlinear analysis, which predicts a final time of arrest and hence fails in describing the subsequent small oscillations, are overcome by the projection approach, as complementary semi-linear direct numerical simulations could confirm (see Appendix B and Integral Multimedia Movie 3).

On the other hand, as visible in Fig. 11(f) [see also Fig. 7(a)], when a pure hysteresis at zero speed is considered, there exists a final time of arrest for which $\dot{e} = 0$ and $e = e_{eq}^{final} \neq e_{eq}^{initial}$, which results in a new final equilibrium. In the test cases of Figs. 8 and 11(b) and 11(d), e_{eq}^{final} is very small, leading to a final static contact angle $\theta^{final} \approx 91^\circ$ vs an initial static angle $\theta_s = 90^\circ$. However, this may not be always the case as e_{eq}^{final} mainly depends on the imposed initial condition and, particularly, on the width of the prescribed hysteresis range, Δ . Although a thorough parametric analysis should be carried out in order to investigate the range of the possible e_{eq}^{final} , Eq. (26) says that, once Δ is assigned, $\max(|e_{eq}^{final}|)$ is bounded by $F_0 \Delta / 2$, with a maximum static angle $\theta = \theta_s \pm \Delta / 2$.

VI. CONCLUSION

In this paper, we have presented a mathematical model based on successive linear eigenmode projections, which induce a loss of total energy and eventually contributes to the progressive nonlinear damping in the liquid motion. The projection scheme allowed us to describe and reproduce the nonlinear contact line dynamics

and fluid bulk motion in confined basins and in the limit of small oscillation amplitudes, for which the expansion (13) holds. We have shown how, through the projection scheme, the actual dynamical change in the contact line boundary condition can be accounted for, thus overcoming the limitation of the asymptotic model. The computed instantaneous damping rate and frequency, which show a progressive transition from the initial stick-slip contact line motion, subjected to solid-like friction, to a final pinned state with fluid bulk oscillations damped by viscous dissipation solely, are in qualitative agreement with previous experimental observations.^{8,16}

In order to formalize the projection method presented here, a series of simplifications have been introduced throughout the paper. The static contact angle was assumed equal to $\pi/2$, for which the free-surface at rest is flat. Moreover, the contact line model was considered to be symmetric with respect to the zero contact line speed axis, although experimental evidence [see Fig. 1(a)] shows that the advancing and receding dynamics usually differ from each other. Notwithstanding such idealizations, there are no actual restrictions in considering a nonflat static free-surface, i.e., small oscillation on the top of a static meniscus $\eta_0 \neq 0$ ($\theta_s \neq \pi/2$) or in assuming non-symmetric advancing and receding phases (asymmetric contact line law).

Although the asymptotic model was shown to be only meaningful in the first phase of the overall dynamics, its greatest advantage, together with the reduced computational cost, is the straightforward application to any nonlinear contact line model of experimental inspiration. We have thus shown how the projection method can be generalized to any smooth nonlinear function, e.g., a cubic law, preserving high accuracy in the final results, as shown by the comparison with semi-linear direct numerical simulations (see Appendix B and Integral Multimedia Movie 3). In reality, the static hysteresis range often exists, but at the same time the angle does not vary linearly with the contact line speed (for $\dot{e} \neq 0$) as in Hocking's law, but rather nonlinearly and likely as in Jiang *et al.* model. Therefore, a combination of the two models, which together reduce to Dussan's law,⁹ could be in principle more realistic [see Fig. 1(a)].

Despite the two-dimensional idealization and the semi-linear structure of the equations (owing to the small perturbation assumption), the contact line model is nonlinear, especially in the pure hysteresis case, and makes the system numerically stiff. As a consequence, a direct numerical simulation of the equations would require an implicit temporal integration scheme with a small time step in order to both preserve numerical stability and accuracy, thus yielding a high computational cost. Although the projection algorithm solves the same full set of equations, its computational cost is very advantageous with respect to a standard numerical time integration since only few eigenvalues calculations are needed. Indeed, the temporal evolution is obtained by advancing in time linear quantities (known *a priori* from the eigen-calculation) according to their decay rate and oscillation frequency and whose corresponding amplitudes are easily computed at each transition by exploiting the bi-orthogonality relation of direct and adjoint modes (see also supplementary material). Therefore, the projection approach can also be seen as an efficient physics-based reduced order model for the underlying small-amplitude nonlinear dynamics. A quantitative comparison with experimental observations was not possible due to the simplistic two-dimensional case considered, which drastically

simplifies the formulation. In fact, the transition criterion for the consecutive projections is univocally defined by the motion of the contact line, which in two-dimension actually reduces to a contact point, following the prescribed law. In three-dimension, different points along the air–liquid–solid triple line have different velocities and the contact angle becomes a function of the contact line coordinate. Thus, the three-dimensionality breaks the uniqueness of the transition criterion, making the extension to three-dimensional vessels challenging. Nevertheless, we underline that the model could be straightforwardly applied to axisymmetric dynamics, where all the points along the interface perimeter behave in the same manner (two-dimensional-like model), as in the case of liquid oscillations in the U-tube configuration recently investigated in Ref. 16, for which quantitative comparison with experiments would be in principle possible.

SUPPLEMENTARY MATERIAL

See the [supplementary material](#) for details on the adjoint problem and adjoint modes derivation. A thorough convergence and error analysis, including further clarification about the treatment of the lateral wall boundary condition (i.e., slip length model vs no-slip model in the pinned-phase), is also given in the supplementary notes.

AUTHOR DECLARATIONS

Conflict of Interest

The author have no conflicts to disclose.

DATA AVAILABILITY

The data that support the findings of this study are available from the corresponding author upon reasonable request.

APPENDIX A: CONVERGENCE ANALYSIS OF THE EIGEN-CALCULATION

The convergence analysis of the eigenvalue calculation in the case of Hocking's model with hysteresis, i.e., free-phase and pinned-phase, is given in [Table I](#) for three relevant eigenvalues, $n, m = 1, 15$, and 30 (note that the truncation number of the series is $N = 30$) and four different mesh refinements. The maximum error is seen to be on the damping of mode $n, m = 30$ and to decrease below 3% for $n_x = n_z = 80$, which is considered a satisfactory trade-off between computation efficiency and accuracy. We underline that the time step used to march in time all our simulations was set to $\Delta t = 0.005$. This value is ten times smaller than the shortest oscillation period, $T_{pm=30} \approx 0.05$, hence ensuring that no modes are filtered out artificially.

APPENDIX B: VALIDATION VIA COMPARISON WITH SEMI-LINEAR DNS

The more sophisticated and discretized projection scheme employed in the case of the Jiang *et al.* cubic model is validated by comparison with semi-linear direct numerical simulation. Governing equations and boundary conditions (1)–(5), linearized around

TABLE I. Convergence analysis for the free and pinned eigenvalue calculations in the case of [Figs. 11\(b\), 11\(d\), and 11\(f\)](#) with $Bo = 50$, $Re = 7\,367$, $Ca = 0.0068$, and $\alpha = 77$ rad. n_x and n_z denote the number of grid points in the x and z directions, respectively. Three relevant eigenvalues, $\lambda = \sigma + i\omega$ with $n, m = 1, 15$, and 30 ($N = 30$), are shown.

$n_x = n_z$	λ_{f1}	λ_{f15}	λ_{f30}	max (e_σ, e_ω)
50	$-0.027 + i\,1.29$	$-1.200 + i\,43.9$	$-2.738 + i\,124.9$	\dots
60	$-0.027 + i\,1.29$	$-1.219 + i\,44.1$	$-3.138 + i\,125.9$	14.6%
70	$-0.027 + i\,1.29$	$-1.224 + i\,44.2$	$-3.238 + i\,126.6$	3.2%
80	$-0.027 + i\,1.29$	$-1.219 + i\,44.2$	$-3.299 + i\,126.9$	1.9%
	λ_{p1}	λ_{p15}	λ_{p30}	
50	$-0.001 + i\,1.47$	$-0.474 + i\,45.2$	$-1.737 + i\,125.8$	\dots
60	$-0.001 + i\,1.47$	$-0.489 + i\,45.3$	$-1.844 + i\,127.2$	6.2%
70	$-0.001 + i\,1.47$	$-0.497 + i\,45.4$	$-1.936 + i\,127.8$	4.9%
80	$-0.001 + i\,1.47$	$-0.497 + i\,45.4$	$-1.992 + i\,128.1$	2.9%

the rest state $\mathbf{q}_0 = \{0, -z, 0\}^T$, but subjected to the nonlinear contact line model, e.g., a cubic law, can be written in compact matrix form as

$$(\partial_t M - K) \mathbf{q}_1 = \mathbf{F}(\partial_t \eta_1|_{x=\pm 1}), \quad (\text{B1})$$

where M and K are, respectively, the mass matrix and the stiffness matrix implemented numerically. The forcing vector \mathbf{F} contains the nonlinear part of the contact line model and hence it has non-zero components at the contact line only,

$$M = \begin{bmatrix} I_u & 0 & 0 \\ 0 & 0 & 0 \\ 0 & 0 & I_\eta \end{bmatrix}, \quad K = \begin{bmatrix} Re^{-1} \Delta & -\nabla & 0 \\ \nabla^T & 0 & 0 \\ -I_{w|z=0} & 0 & 0 \end{bmatrix}, \quad (\text{B2})$$

and I_u, I_η are the identity matrices associated to \mathbf{u} and η .

We note that the very same matrices have been implemented numerically in order to solve the eigenvalue problem in the different phases of the projection algorithm, i.e., we solved $[(\sigma + i\omega)M - K] \hat{\mathbf{q}} = \mathbf{0}$ with the proper boundary conditions.

Equation (B1) is discretized in space by means of a pseudospectral Chebyshev collocation method and integrated in time with the implicit backward differentiation formula of order 2. The discretized state vector at the n th time step is obtained by solving the nonlinear equation,

$$\frac{3}{2} M \mathbf{q}_1^n - 2 M \mathbf{q}_1^{n-1} + \frac{1}{2} M \mathbf{q}_1^{n-2} - \Delta t K \mathbf{q}_1^n = \Delta t \mathbf{F}(\partial_t \eta_1|_{x=\pm 1}), \quad (\text{B3})$$

with $\partial_t \eta_1|_{x=\pm 1} = (\frac{3}{2} \eta_1^n - 2 \eta_1^{n-1} + \frac{1}{2} \eta_1^{n-2})|_{x=\pm 1}$.

The linearization around the base-flow \mathbf{q}_0 implicitly assumes that nonlinear inertial and free-surface curvature terms are negligible (only the contact line nonlinearity is kept for small oscillation amplitudes). As a consequence, the computational domain is kept fixed in time and it is defined by the flow configuration at rest. In [Fig. 12](#), the interface shape computed via projection scheme and semi-linear direct numerical simulation is shown for three different and equi-spaced time instants of the nonlinear evolution discussed in [Figs. 11\(a\), 11\(c\), and 11\(e\)](#), resulting in a quantitative very good agreement.

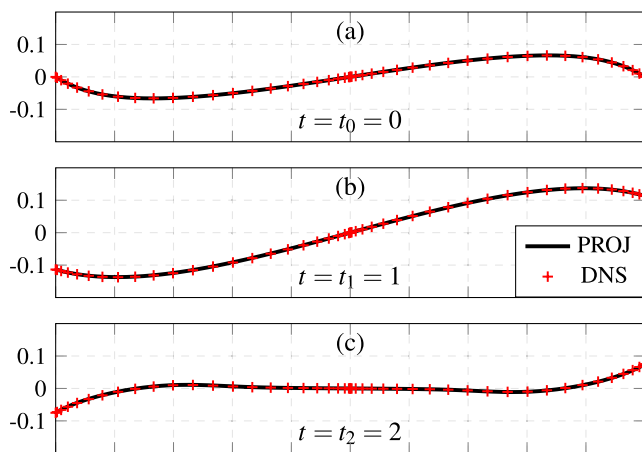


FIG. 12. Black solid line: free-surface shape corresponding to the nonlinear time evolution presented in Fig. 11 (Jiang *et al.* cubic contact line law) and obtained via projection algorithm at three different non-dimensional time instants, (a) $t = t_0 = 0$, (b) $t = t_1 = 1$, and (c) $t = t_2 = 2$. Red crosses: semi-linear direct numerical simulation, advanced in time with the same time step, i.e., $\Delta t = 0.005$. See also Integral Multimedia Movie 3 associated with Figs. 11(a) and 11(c).

APPENDIX C: THE CRUCIAL ROLE OF VISCOSITY IN THE CONVERGENCE OF THE PROJECTION SCHEME

To ease the mathematical treatment of the lateral wall boundary condition during the free-phase, in this paper, a simple perfect slip condition was assumed. When the contact line is free to slide (free-phase), e.g., according to Hocking's linear law, the total damping coefficient is produced by the sum of four sources, namely, (i) the fluid bulk, (ii) the solid bottom, (iii) the sidewall, and (iv) the contact line,^{2,4,10}

$$\sigma_{\text{free}} = \sigma_{\text{bulk}} + \sigma_{\text{bottom}} + \sigma_{\text{side}} + \sigma_{\text{cl}}. \quad (\text{C1})$$

In this work, σ_{side} is overlooked owing to the imposition of a stress-free condition. Moreover, if the ratio h/L is sufficiently large (as, for example, in the test cases proposed in our paper), then the bottom term is negligible. In a vast range of typical lab-working conditions (except for highly viscous fluids or for very shallow fluid layers), the contact line dissipation represents the dominant term, i.e., $\sigma_{\text{cl}} \gg \sigma_{\text{bulk}}$ (see Refs. 5 and 10, among other references) so that $\sigma_{\text{free}} \approx \sigma_{\text{cl}}$. Hence, one may think that an inviscid model supplemented with a contact line law, as originally proposed by Hocking,¹⁰ would be adequate to describe the free contact line dynamics and, at the same time, it would be much simpler than the present viscous formulation. The inviscid weakly nonlinear analysis presented in Ref. 14, where only the leading order free contact line dynamics is described, was indeed formalized in this spirit.

Whereas this reasoning applies to the free-dynamics, it should be noted that during the pinned-phase, the contact line is at rest so that no contact line dissipation takes place at all, i.e., $\sigma_{\text{cl}} = 0$. During such a phase, the overall dissipation is given by (i) bulk, (ii) bottom (negligible in the deep water regime), and (iii) sidewall. Although we are neglecting this main contribution (iii) (see [supplementary material](#) for a thorough discussion about the stress-free vs no-slip

lateral wall condition accounting for (iii) during the pinned phase), the remaining bulk dissipation plays a crucial role in our projection scheme that aims at describing the full dynamics, i.e., transition from stick-slip to pinned.

The bulk dissipation is indeed approximately proportional to the square of the wave natural frequency, ω^2 (it was proven for a free contact line,^{2,4} but it qualitatively applies for a pinned dynamics), meaning that the bulk damping can certainly be very small for the lowest frequency modes, yet, it tends to rapidly increase for higher frequency modes. Figure 10 (associated with the case discussed in Fig. 8) shows how the convergence of the projection algorithm is well achieved by retaining the first 30 free and pinned modes. This is possible exactly because the linear damping (bottom + bulk + contact line in the free-phase and bottom + bulk in the pinned phase) damps out higher frequency modes rapidly enough, i.e., before they are projected again on the next phase, hence ensuring the series and thus the method convergence for a finite number of modes, N (truncation number). On the contrary, if an inviscid model was to be considered, the free-modes used to initialize the dynamics would project at the first transition on several pinned modes. None of the latter modes, due to the lack of dissipative sources, would die out during the pinned phase; hence, all of them would project back on the next free phase modes. At each free-to-pinned projection, many unphysical pinned modes would be excited, preventing the convergence of the algorithm and describing an unrealistic “ultraviolet catastrophe.” Furthermore, even if the loss of energy taking place at each projection and ascribed to the nonlinear static hysteresis range eventually led the contact line to pin, the final pinned oscillations would last indefinitely, as no dissipation is present without viscosity.

To conclude, keeping viscosity, albeit small, is not a mere choice but rather a fundamental aspect that is required to ensure that the method works properly and that it is capable to reproduce a behavior closer to the actual one observed in real experiments.

REFERENCES

- ¹H. Lamb, *Hydrodynamics* (Cambridge University Press, 1993).
- ²K. M. Case, and W. C. Parkinson, “Damping of surface waves in an incompressible liquid,” *J. Fluid Mech.* **2**, 172–184 (1957).
- ³F. Ursell, “Edge waves on a sloping beach,” *Proc. R. Soc. Lond.* **214**, 79–97 (1952).
- ⁴J. W. Miles, “Surface-wave damping in closed basins,” *Proc. R. Soc. Lond.* **297**, 459–475 (1967).
- ⁵T. B. Benjamin, and F. J. Ursell, “The stability of the plane free surface of a liquid in vertical periodic motion,” *Proc. R. Soc. Lond.* **225**, 505–515 (1954).
- ⁶G. H. Keulegan, “Energy dissipation in standing waves in rectangular basins,” *J. Fluid Mech.* **6**, 33–50 (1959).
- ⁷B. Cocciano, S. Faetti, and M. Nobili, “Capillarity effects on surface gravity waves in a cylindrical container: Wetting boundary conditions,” *J. Fluid Mech.* **231**, 325–343 (1991).
- ⁸B. Cocciano, S. Faetti, and C. Festa, “Experimental investigation of capillarity effects on surface gravity waves: Non-wetting boundary conditions,” *J. Fluid Mech.* **246**, 43–66 (1993).
- ⁹E. B. Dussan, “On the spreading of liquids on solid surfaces: Static and dynamic contact lines,” *Annu. Rev. Fluid Mech.* **11**, 371–400 (1979).
- ¹⁰L. M. Hocking, “The damping of capillary-gravity waves at a rigid boundary,” *J. Fluid Mech.* **179**, 253–266 (1987).
- ¹¹O. V. Voinov, “Hydrodynamics of wetting,” *Fluid Dyn.* **11**, 714–721 (1976).

- ¹²R. G. Cox, "The dynamics of the spreading of liquids on a solid surface. Part 1. Viscous flow," *J. Fluid Mech.* **168**, 169–194 (1986).
- ¹³H. B. Eral, J. C. M. T. Mannerje, and J. M. Oh, "Contact angle hysteresis: A review of fundamentals and applications," *Colloid Polym. Sci.* **291**, 247–260 (2013).
- ¹⁴F. Viola, P.-T. Brun, and F. Gallaire, "Capillary hysteresis in sloshing dynamics: A weakly nonlinear analysis," *J. Fluid Mech.* **837**, 788–818 (2018).
- ¹⁵F. Viola, and F. Gallaire, "Theoretical framework to analyze the combined effect of surface tension and viscosity on the damping rate of sloshing waves," *Phys. Rev. Fluids* **3**, 094801 (2018).
- ¹⁶B. Dollet, É. Lorenceau, and F. Gallaire, "Transition from exponentially damped to finite-time arrest liquid oscillations induced by contact line hysteresis," *Phys. Rev. Lett.* **124**, 104502 (2020).
- ¹⁷T. B. Benjamin, and J. C. Scott, "Gravity-capillary waves with edge constraints," *J. Fluid Mech.* **92**, 241–267 (1979).
- ¹⁸J. Graham-Eagle, "A new method for calculating eigenvalues with applications to gravity-capillary waves with edge constraints," *Math. Proc. Camb. Phil. Soc.* **94**, 553–564 (1983).
- ¹⁹J. T. Stuart, "On the non-linear mechanics of wave disturbances in stable and unstable parallel flows. Part 1. The basic behaviour in plane Poiseuille flow," *J. Fluid Mech.* **9**, 353–370 (1960).
- ²⁰D. Jiang, C. Pierre, and S. W. Shaw, "Large-amplitude non-linear normal modes of piecewise linear systems," *J. Sound Vib.* **272**, 869–891 (2004).
- ²¹E. H. Moussi, S. Bellizzi, B. Cochelin, and I. Nistor, "Nonlinear normal modes of a two degrees-of-freedom piecewise linear system," *Mech. Syst. Signal Process.* **64**, 266–281 (2015).
- ²²E. Pesheck, C. Pierre, and S. W. Shaw, "A new Galerkin-based approach for accurate non-linear normal modes through invariant manifolds," *J. Sound Vib.* **249**, 971–993 (2002).
- ²³S. W. Shaw, and C. Pierre, "Normal modes of vibration for non-linear continuous systems," *J. Sound Vib.* **169**, 319–347 (1994).
- ²⁴S. W. Shaw, and C. Pierre, "Normal modes for non-linear vibratory systems," *J. Sound Vib.* **164**, 85–124 (1993).
- ²⁵A. Vakakis, "Non-linear normal modes (NNMS) and their applications in vibration theory: An overview," *Mech. Syst. Signal Process.* **11**, 3–22 (1997).
- ²⁶C. L. M. H. Navier, "Mémoire sur les lois du mouvement des fluides," *Mém. Acad. R. Sci. Inst. France* **6**, 389–440 (1823).
- ²⁷E. Lauga, M. Brenner, and H. Stone, *Microfluidics: The No-Slip Boundary Condition*, Springer Handbook of Experimental Fluid Mechanics (Springer Berlin Heidelberg, 2007), pp. 1219–1240.
- ²⁸C. Huh, and L. E. Scriven, "Hydrodynamic model of steady movement of a solid/liquid/fluid contact line," *J. Colloid. Interf. Sci.* **35**, 85–101 (1971).
- ²⁹S. H. Davis, "On the motion of a fluid-fluid interface along a solid surface," *J. Fluid Mech.* **65**, 71–95 (1974).
- ³⁰J. Miles, "Capillary-viscous forcing of surface waves," *J. Fluid Mech.* **219**, 635–646 (1990).
- ³¹C.-L. Ting, and M. Perlin, "Boundary conditions in the vicinity of the contact line at a vertically oscillating upright plate: An experimental investigation," *J. Fluid Mech.* **295**, 263–300 (1995).
- ³²L. Jiang, M. Perlin, and W. W. Schultz, "Contact-line dynamics and damping for oscillating free surface flows," *Phys. Fluids* **16**, 748–758 (2004).
- ³³G. W. Young, and S. H. Davis, "A plate oscillating across a liquid interface: Effects of contact-angle hysteresis," *J. Fluid Mech.* **174**, 327–356 (1987).
- ³⁴P. Meliga, J. M. Chomaz, and D. Sipp, "Global mode interaction and pattern selection in the wake of a disk: A weakly nonlinear expansion," *J. Fluid Mech.* **633**, 159–189 (2009).
- ³⁵A. Bongarzone, A. Bertsch, P. Renaud, and F. Gallaire, "Impinging planar jets: Hysteretic behaviour and origin of the self-sustained oscillations," *J. Fluid Mech.* **913**, A51 (2021).
- ³⁶A. H. Nayfeh, *Perturbation Methods* (Wiley, 2008).